

TM scattering by a metallic half plane with a resistive sheet extension

Leo C. Kempel and John L. Volakis

April 10, 1992

Abstract

An analysis is presented of the scattering by a resistive strip joined to a metallic half plane. Three different solutions are developed, one of which is exact and is based on the moment method/Green's function approach. The other two are approximations, one of which improves as the resistive strip width decreases whereas the other does the same for large strip widths. Using the moment method solution as a reference, the accuracy of each approximation is examined and guidelines for using them are developed. It is found that the validity ranges of two approximations overlap, making them suitable for computing the TM scattering of the configuration regardless of the strip's width and resistivity.

Eng

UMRO411

1 Introduction

Resistive sheets or cards are often used on modern aircraft for controlling the scattering by a variety of surface discontinuities including those associated with apertures, leading and trailing edges, and antennas. For such applications the resistive sheet is placed in front of or around a metallic truncation in a manner which depends on the shape of the metallic geometry and the desired control. Perhaps the simplest among such configurations is a metallic half plane loaded with a resistive strip extension as illustrated in Figure 1, and the purpose of this paper is to present a rather thorough characterization of the scattering by such a loaded half plane. Our aim is to derive simple and efficient solutions not associated with extensive computational demands.

Three different solutions are presented and discussed from the point of view of accuracy, efficiency and computational requirements. The first is based on the moment method (MM)/Green's function approach and parallels the solution given by Newman [1] for a dielectric strip in the presence of a metallic half plane. Our solution, though, employs a different procedure for the evaluation of the diagonal and non-diagonal impedance matrix elements, and this is important in keeping the computational requirements to a minimum. Specifically, the integrand associated with the diagonal elements is herein regularized differently leading to definite rather than infinite integrals. Also, because the resistive strip extension and the metallic half plane occupy the same plane, the resulting non-diagonal matrix elements can be expressed in terms of definite integrals. Consequently, the impedance matrix fill time is kept at a minimum.

The other two scattering solutions are approximations, one being valid for small width resistive strip extensions whereas the other is a high frequency solution. The small width approximation is obtained by noting that for small width sheet extensions, the current amplitude can be analytically described to within a constant. This constant is subsequently determined by inserting the proposed analytical expression into the exact integral equation. The limitations of this approximation for determining the echowidth of the subject configuration for different complex sheet resistivities and as the width increases is discussed in the results section of the paper. There, we present guidelines where this approximation is most accurate and suitable for engineering calculations.

The high frequency solution for a single strip extension follows the formal

procedure outlined by Herman and Volakis in [2] and includes up to third order diffraction contributions. However, the solution in [2] applies to an isolated resistive strip whereas here the strip is joined with a metallic half plane, requiring a different diffraction coefficient at this junction. Such a diffraction coefficient is given in [3], and upon relating it to the diffraction coefficient for the isolated resistive half plane, the higher order diffracted fields for the subject configuration are obtained by making simple modifications of the results in [2]. The derived high frequency solution is validated by comparison with the MM/Green's function solution. Specifically, several computations are presented which demonstrate the solution's accuracy and limitation as the width of the strip extension becomes smaller. The high frequency solution for sheet extensions comprised of multiple resistive strips is also discussed.

2 Integral equation formulation

Consider the plane wave

$$E_z^i = e^{jk_0(x \cos \phi_0 + y \sin \phi_0)} \quad (1)$$

which illuminates a metallic half plane whose front edge is loaded by a resistive strip as shown in Figure 1. The metallic section of the half plane occupies the $x > 0$ portion of the $y = 0$ plane, whereas the resistive strip extends from $x = -w$ to the edge of the metal ($x = 0$) also in the $y = 0$ plane.

We are interested in computing the scattered field from this configuration due to the excitation (1). A convenient way for accomplishing this is to employ the MM/Green's function approach also employed by Newman [1], who considered the scattering of a dielectric cylinder in the presence of a metallic half plane. Based on this procedure, the presence of the half plane is accounted for by introducing the Green's function of the metallic half plane, thus eliminating a need to explicitly introduce and compute the currents excited on that portion of the half plane. The problem then reduces to that of determining the resistive strip currents. The associated integral equation for the strip currents can be found by imposing the boundary condition

$$E_z = Z_0 R_e(x) J_z(x) \quad -w < x < 0, \quad y = 0. \quad (2)$$

In this, E_z denotes the total field, $J_z(x)$ is the strip current, Z_0 is the free space intrinsic impedance and $R_e(x)$ is the normalized resistivity profile of the strip.

The total field E_z is comprised of three contributions. They include the unperturbed incident field (1), the field scattered by the metallic half plane in isolation (E_z^{HP}) and that caused by the radiation of the strip currents in the presence of the metallic half plane. From [5,6] we have that

$$\begin{aligned} E_z^i(\rho, \phi) + E_z^{\text{HP}}(\rho, \phi) &= E_z^{\text{go}}(\rho, \phi, \phi_0) \\ &= e^{\frac{j\pi}{4}} \frac{e^{-jk\rho}}{\sqrt{\pi}} \left[F_c \left(-\sqrt{2\pi\rho} \cos \frac{\phi - \phi_0}{2} \right) \right. \\ &\quad \left. - F_c \left(-\sqrt{2\pi\rho} \cos \frac{\phi + \phi_0}{2} \right) \right] \end{aligned} \quad (3)$$

in which (ρ, ϕ) denote the usual cylindrical coordinates of the observation point and $F_c(z)$ is Clemmow's transition function [7]

$$F_c(z) = e^{jz^2} \int_z^\infty e^{-j\tau^2} d\tau. \quad (4)$$

It satisfies the identity

$$F_c(z) + F_c(-z) = \sqrt{\pi} e^{\frac{-j\pi}{4}} e^{jz^2}, \quad (5)$$

which can be used to recover the incident and reflected fields from (3). When the argument of $F_c(z)$ is positive (and real) we may relate it to the Kouyoumjian-Pathak [8] transition function $F_{kp}(z)$ via the relation

$$F_c(|z|) = \frac{F_{kp}(z^2)}{2j|z|}. \quad (6)$$

Thus, by invoking (5) the computation of $F_c(z)$ amounts to evaluating the Kouyoumjian-Pathak transition function, which is well documented.

To find the field generated by the strip current in the presence of the metallic half plane we first consider that radiated by a line source of unit amplitude. This is the Green's function of the configuration and with the source in the $y = 0$ plane it is given by [5,6]

$$G_E(\rho, \phi; x') = \frac{e^{-jk_0 R}}{2\pi} \int_{-p}^p \frac{e^{-ju^2}}{\sqrt{u^2 + 2k_0 R}} du \quad (7)$$

where

$$R = \sqrt{\rho^2 + \chi'^2 + 2\rho\chi' \cos \phi}, \quad (8)$$

$$p = 2\sqrt{\frac{k_0\rho\chi'}{\rho + \chi' + R}} \sin \frac{\phi}{2} \quad (9)$$

and

$$\chi' = |x'| \quad (10)$$

denotes the distance of the line source from the half plane edge. The field radiated by the strip current can now be expressed as

$$E_z^{sr}(\rho, \phi) = -jk_0 Z_0 \int_{-w}^0 J_z(x') G_E(\rho, \phi; x') dx' \quad (11)$$

with the total field given by

$$E_z = E_z^i + E_z^{\text{HP}} + E_z^{sr} = E_z^{\text{go}} + E_z^{sr}. \quad (12)$$

Substituting this into (2) yields the integral equation

$$Y_0 E^{\text{go}}(\rho = \chi, \phi_0, \phi = \pi) = R_e(x) J_z(x) + jk_0 \int_{-w}^0 J_z(x') G_E(x; x') dx' \quad (13)$$

where $G_E(x; x') = G_E(\rho = |x| = \chi, \phi = \pi; x')$ and $Y_0 = \frac{1}{Z_0}$. The solution of this integral equation is considered in the next section.

3 Integral equation solution

One of the simplest procedures for discretizing the integral equation (13) is to employ point matching with pulse-basis expansion functions. Using N subdomains for discretizing the strip extension and testing at the center of each of these yields the standard system

$$[Z_{mn}][J_n] = [V_m]. \quad (14)$$

In this, J_n denotes the amplitude of the n th pulse centered at $x_n = -w + n\Delta/2$ with $n = 1, 2, \dots, N$ and Δ being the width of the subdomain. Also,

$$V_m = V(x_m) = Y_0 E_z^{\text{go}}(\rho = |x_m|, \phi_0, \phi = \pi) \quad (15)$$

and the impedance matrix elements are formally given by

$$Z_{mn} = \begin{cases} R_e(x_m) + \tilde{Z}_{mn} & m = n \\ \tilde{Z}_{mn} & m \neq n \end{cases} \quad (16)$$

$$\tilde{Z}_{mn} = \frac{jk_0}{2\pi} \int_{x_n-\Delta/2}^{x_n+\Delta/2} dx' e^{-jk_0 R_m(x')} \int_{-p}^p \frac{e^{-ju^2} du}{\sqrt{u^2 + 2k_0 R_m(x')}} \quad (17)$$

with $R_m(x') = |\chi_m - \chi'|$ and

$$p = \begin{cases} \sqrt{2k_0 \chi'} & \chi_m > \chi' \\ \sqrt{2k_0 \chi_m} & \chi_m < \chi'. \end{cases}$$

For $m \neq n$ the matrix elements \tilde{Z}_{mn} can be readily evaluated numerically. However, when $m = n$, $R_m(x')$ vanishes making the integrand singular over the range of integration. This makes it necessary for an analytical treatment of the integral and the standard approach is to isolate the singularity in some integrand which can be evaluated analytically. Newman [1] chose a certain procedure based on this principle but his final non-singular integrals involved infinite limits making their evaluation time-consuming and cumbersome.

Herewith, we employ a different approach for isolating and treating the singularity and this results in a more efficient and simpler evaluation of \tilde{Z}_{mm} . We begin by rewriting \tilde{Z}_{mm} as

$$\tilde{Z}_{mm} = \frac{jk_0}{2\pi} \int_{x_n-\Delta/2}^{x_n+\Delta/2} dx' \left\{ \int_{-p}^p \frac{(e^{-j[u^2 + k_0 R_m(x')]}) - 1}{\sqrt{u^2 + 2k_0 R_m(x')}} du + \tilde{I}_m(x') \right\} \quad (18)$$

where

$$\tilde{I}_m(x') = \int_{-p}^p \frac{du}{\sqrt{u^2 + 2k_0 R_m(x')}} = \ln \left[\frac{\sqrt{p^2 + 2k_0 R_m(x')} + p}{\sqrt{p^2 + 2k_0 R_m(x')} - p} \right]. \quad (19)$$

Using (9), the integral $\tilde{I}_m(x')$ can be further simplified to read

$$\tilde{I}_m(x') = \ln \left| \frac{\sqrt{\chi'} + \sqrt{\chi_m}}{\sqrt{\chi'} - \sqrt{\chi_m}} \right| \quad (20)$$

and its expected logarithmic singularity is now apparent. This is, of course, an integrable singularity. In particular, we have

$$\int_{x_n-\Delta/2}^{x_n+\Delta/2} \tilde{I}_m(x') dx' = +2 \int_{-(x_n+\Delta/2)}^{(x_n-\Delta/2)} \tilde{\chi}' \ln \left| \frac{\tilde{\chi}_m + \tilde{\chi}'}{\tilde{\chi}_m - \tilde{\chi}'} \right| d\tilde{\chi}'$$

where $\tilde{\chi}_m = \sqrt{\chi_m} = \sqrt{|x_m|}$ and $\tilde{\chi}' = \sqrt{\chi} = \sqrt{|x'|}$. The last integral can be readily evaluated analytically and on doing so, \tilde{Z}_{mm} can be rewritten as

$$\tilde{Z}_{mm} = \frac{jk_0}{2\pi} \left[\int_{x_n-\Delta/2}^{x_n+\Delta/2} dx' \left\{ \int_{-p}^p \frac{(e^{-j[u^2+k_0 R_m(x')]} - 1) du}{\sqrt{u^2 + 2k_0 R_m(x')}} + \tilde{\zeta}_{mm} \right\} \right] \quad (21)$$

with $\tilde{\zeta}_{mm}$ given by

$$\begin{aligned} \tilde{\zeta}_{mm} &= (\tilde{\chi}_m)^2 \ln \left[\frac{(\tilde{\chi}_m + \tilde{\chi}_m^+)(\tilde{\chi}_m^- - \tilde{\chi}_m)}{(\tilde{\chi}_m + \tilde{\chi}_m^-)(\tilde{\chi}_m - \tilde{\chi}_m^+)} \right] \\ &\quad - (\chi_m^+)^2 \ln \left[\frac{\tilde{\chi}_m + \tilde{\chi}_m^+}{\tilde{\chi}_m - \tilde{\chi}_m^+} \right] - (\chi_m^-)^2 \ln \left[\frac{\tilde{\chi}_m^- - \tilde{\chi}_m}{\tilde{\chi}_m^- + \tilde{\chi}_m} \right] \\ &\quad + 2\tilde{\chi}_m(\tilde{\chi}_m^- - \tilde{\chi}_m^+). \end{aligned} \quad (22)$$

Consistent with our notation, $\tilde{\chi}_m^\pm = \sqrt{|x_m \pm \Delta/2|}$.

A numerical evaluation of \tilde{Z}_{mm} can now be readily performed and in particular we found that a four point Gaussian quadrature was sufficient for each line integral in (21) and (17).

Once $J_z(x)$ is determined, the far gone scattered field is given by

$$E_z^s(\rho \rightarrow \infty, \phi) = E_z^{\text{HP}}(\rho \rightarrow \infty, \phi) + E_z^{sr}(\rho \rightarrow \infty, \phi). \quad (23)$$

Since $F_{kp}(z \rightarrow \infty) = 1$ from (3), (5) and (6) we find that

$$E_z^{\text{HP}}(\rho \rightarrow \infty, \phi) = \frac{e^{-jk\rho}}{\sqrt{\rho}} \frac{e^{-j\frac{\pi}{4}}}{\sqrt{2\pi k_0}} \frac{2 \sin \frac{\phi}{2} \sin \frac{\phi_0}{2}}{\cos \phi + \cos \phi_0} - e^{-jk_0 \rho \cos(\phi + \phi_0)} U(\pi - \phi - \phi_0) \quad (24)$$

with $U(x)$ being the unit step function. Thus the second term of this expression simply represents the reflected field from the metallic half plane. For the far zone evaluation of E_z^{sr} we note that

$$G_E(\rho \rightarrow \infty, \phi; x') = \frac{e^{-jk_0(\rho + \chi' \cos \phi)}}{2\pi \sqrt{2k_0 \rho}} \int_{-\sqrt{2k_0 \chi' \sin \frac{\phi}{2}}}^{\sqrt{2k_0 \chi' \sin \frac{\phi}{2}}} e^{-ju^2} du, \quad (25)$$

which on using the definition (4) can be written as

$$G_E(\rho \rightarrow \infty, \phi; x') = \frac{e^{-jk_0\rho}}{\sqrt{\rho}} \frac{e^{-jk_0x'}}{2\pi\sqrt{2k_0}} \left[F_c \left(-2\sqrt{k_0\chi'} \sin \frac{\phi}{2} \right) - F_c \left(2\sqrt{k_0\chi'} \sin \frac{\phi}{2} \right) \right]. \quad (26)$$

Substituting this into (13) we can express the far zone scattered field from the subject configuration as

$$\begin{aligned} E^s(\rho, \phi) = & \frac{e^{-jk_0\rho}}{\sqrt{\rho}} \left\{ \frac{e^{-\frac{j\pi}{4}}}{\sqrt{2\pi k_0}} \frac{2 \sin \frac{\phi}{2} \sin \frac{\phi_0}{2}}{\cos \phi + \cos \phi_0} \right. \\ & + \frac{jZ_0}{2\pi} \sqrt{\frac{k_0}{2}} \int_{-w}^0 J_z(x') e^{-jk_0x'} \\ & \cdot \left[F_c \left(+\sqrt{2k_0\chi'} \sin \frac{\phi}{2} \right) - F_c \left(-\sqrt{2k_0\chi'} \sin \frac{\phi}{2} \right) \right] dx'. \quad (27) \end{aligned}$$

In this, we have excluded the contribution of the reflected/specular half plane field which is of interest only for bistatic computations.

4 Approximate solution for narrow strip extension

When the width of the resistive strip extension is small, it is possible to represent the current density $J_z(x)$ with a simple analytical function. From the edge condition, it is already known that at $x = -w$ the current reaches some finite value provided $R_e \neq 0$, whereas at $x = 0$ it can be shown to go to zero as $\sqrt{\chi}$. This is verified in Figure 2 where we plot the modulus of $J_z(x)$ as a function of x for different values of R_e and two incidence angles ($\phi_0 = 60^\circ$ and 130°) as obtained from a solution of (13). It is rather obvious from the curves in Figure 2 that for $w \ll \lambda$ and $R_e \neq 0$, the edge condition at $x = 0$ controls the current density's amplitude behavior over the entire width of the strip extension. That is, $|J_z(x)| \approx A_0\sqrt{\chi}$, where A_0 is a real constant. However, the phase of $J_z(x)$, although it can be taken as constant for small R_e , it is in general a quadratic function of χ whose coefficients are unfortunately a function of R_e .

Based on the above argument, $J_z(x)$ can be expressed as

$$J_z(x) = A(x)\sqrt{\chi} = A_0\sqrt{\chi} e^{j(a_2\chi^2 + a_1\chi + a_0)}. \quad (28)$$

where a_n and A_0 are real constants. Obviously, there is no standard scheme for determining the constants a_n rigorously. Moreover, an attempt to do so will introduce substantial complication, thus defeating our goal to obtain an explicit approximation for the current on the small width strip extension. Instead, we will proceed to solve the integral equation (13) on the assumption that $A(x)$ is a complex constant. This leads to the equation

$$A(x) = \frac{Y_0 E_z^{\text{go}}(\rho = \chi, \phi_0, \phi = \pi)}{R_e \sqrt{\chi} + I(\chi; w)} \quad (29)$$

where

$$I(\chi; w) = \frac{jk_0}{\pi} \left\{ \int_0^\chi \sqrt{\chi'} \int_0^{\sqrt{2k_0\chi'}} \frac{e^{-j(u^2 + k_0|\chi - \chi'|)}}{\sqrt{u^2 + 2k_0|\chi - \chi'|}} du d\chi' \right. \\ \left. + \int_\chi^w \sqrt{\chi'} \int_0^{\sqrt{2k_0\chi}} \frac{e^{-j(u^2 + k_0|\chi - \chi'|)}}{\sqrt{u^2 + 2k_0|\chi - \chi'|}} du d\chi' \right\} \quad (30)$$

and we have chosen to explicitly show the dependence of A on $\chi = |x|$. As expected, the computed values of A will be different depending on which testing point is chosen. We found that by testing at $\chi = \frac{w}{2}$ (i.e. at the middle of the strip extension), the resulting approximation for $J_z(x)$ yields sufficiently accurate echowidths when $w < \frac{\lambda}{10}$. However an improved approximation which remains valid for strip widths larger than $\frac{\lambda}{10}$ can be attained by enforcing (29) at three different points. Choosing the test points $\chi = \frac{w}{4}, \frac{w}{2}$ and $\frac{3w}{4}$ and using the values of $I(\chi; w)$ from the plots in Figure 4 we can easily determine $A\left(\frac{w}{4}\right)$, $A\left(\frac{w}{2}\right)$ and $A\left(\frac{3w}{4}\right)$. These imply the subsequent approximations

$$a_2 \approx \frac{1}{w^2} \left[8\psi\left(\frac{w}{4}\right) - 16\psi\left(\frac{w}{2}\right) + 8\psi\left(\frac{3w}{4}\right) \right] \quad (31)$$

$$a_1 \approx -\frac{1}{w} \left[10\psi\left(\frac{w}{4}\right) - 16\psi\left(\frac{w}{2}\right) + 6\psi\left(\frac{3w}{4}\right) \right] \quad (32)$$

$$a_0 \approx \frac{1}{w} \left[3\psi\left(\frac{w}{4}\right) - 3\psi\left(\frac{w}{2}\right) + \psi\left(\frac{3w}{4}\right) \right] \quad (33)$$

where $\psi(\chi)$ denotes the phase of $A(\chi)$ and we can set $A_0 = |A\left(\frac{w}{2}\right)|$. The accuracy of the echowidths which result from the current approximation (29) in conjunction with (31)–(33) is undoubtedly a function of the resistivity and the strip extension's width w . It will be quantitatively examined later.

5 High frequency solution for single strip extensions

When the width of the resistive strip extension is large with respect to the wavelength and of constant resistivity R_e , a third order high frequency solution can be employed. This conjecture is directly drawn from a similar high frequency analysis pertaining to an isolated resistive strip [2]. We shall therefore develop a high frequency analysis for the pertinent configuration which accounts for contributions up to and including third order diffraction mechanisms. This analysis will parallel that given in [2] for the isolated resistive strip with the exception that a different diffraction coefficient must be employed for the metal-resistive junction labeled as Q_2 in Figure 4. The pertinent diffraction coefficient for this junction can be extracted from that given by Uzgoren, etc. [3] which applies to an impedance-resistive sheet junction (setting the impedance to zero yields the desired coefficient). On the basis of the solution in [2] and the known diffraction coefficient for the resistive half plane we find that the first order far zone diffracted fields for the pertinent scatterer are

$$E_{z1}^d(\rho, \phi) = \left[D_1(\phi, \phi_0; \eta) + D_2(\phi, \phi_0; \eta) e^{-jk_0 w(\cos \phi + \cos \phi_0)} \right] \frac{e^{-jk\rho}}{\sqrt{\rho}} \quad (34)$$

where

$$D_1(\phi, \phi_0; \eta) = \frac{e^{-\frac{j\pi}{4}}}{\sqrt{2\pi k_0}} \frac{K_+(\phi; \eta) K_+(\phi_0; \eta)}{\cos \phi + \cos \phi_0} \quad (35)$$

and

$$D_2(\phi, \phi_0; \eta) = -2\eta \sin \frac{\phi}{2} \sin \frac{\phi_0}{2} D_1(\pi - \phi, \pi - \phi_0; \eta). \quad (36)$$

Referring to Figure 4, the last are the diffraction coefficients associated with the junctions at Q_1 and Q_2 , respectively, and $K_+(\phi; \eta)$ denotes the Weiner-Hopf split function defined in (5) of [2] with $\eta = 2R_e$.

It is most interesting to note that the diffraction coefficient associated with the metal-resistive junction at Q_2 as given in (36) differs from the resistive half plane diffraction coefficient $D_1(\phi, \phi_0; \eta)$ only by a simple factor and this fact can be exploited in deriving the multiply diffracted fields by simply modifying those given in [2] for the isolated resistive strip. In particular, we

find that the sum of the second order diffracted fields emanating from Q_1 and Q_2 is given by

$$E_{z2}^d(\rho, \phi) = -2\eta \left[\sin \frac{\phi}{2} D_{21}(\pi - \phi, \phi_0; \eta) e^{-jk_0 w \cos \phi_0} + \sin \frac{\phi_0}{2} D_{21}(\phi, \pi - \phi_0; \eta) e^{-jk_0 w \cos \phi} \right] \frac{e^{-jk\rho}}{\sqrt{\rho}} \quad (37)$$

where $D_{21}(\alpha, \beta; \eta)$ is the double diffraction coefficient defined in (52) of [2] and includes possible surface wave contributions.

In a similar manner, the sum of the third order diffracted fields emanating from Q_1 and Q_2 were found to be

$$E_{z3}^d(\rho, \phi) = -2\eta \left[D_{121}(\phi, \phi_0; \eta) e^{-jk_0 w (\cos \phi + \cos \phi_0)} - 2\eta \sin \frac{\phi}{2} \sin \frac{\phi_0}{2} D_{121}(\pi - \phi, \pi - \phi_0; \eta) \right] \frac{e^{-jk\rho}}{\sqrt{\rho}} \quad (38)$$

in which D_{121} is the triple diffraction coefficient given by (62) of [2] with the factor $e^{-jk\rho}/\sqrt{\rho}$ removed. We again remark that $D_{121}(\phi, \phi_0; \eta)$ includes possible surface wave effects present on the resistive strip extension.

The total diffracted field includes the contributions of all diffraction mechanisms and is thus given by the sum

$$E_z^d(\rho, \phi) = E_{z1}^d(\rho, \phi) + E_{z2}^d(\rho, \phi) + E_{z3}^d(\rho, \phi). \quad (39)$$

This should be compared to the scattered field (27) pertinent to the integral equation solution.

6 High Frequency Solution for Multiple Strip Extensions

To develop a high frequency solution for a resistive sheet extension comprised of more than one strip of uniform resistivity, it is necessary to consider a more general solution than that described in the previous section. In particular, it is necessary to modify the first, second and third order diffracted field expressions given for the single strip extension and must also add contributions

from additional mechanisms. The different types of diffraction mechanisms (up to third order) which must be considered are illustrated in Figure 5. The first order diffraction coefficient from two abutting resistive half planes has been derived in [4] and by using the parameters defined in Figure 5(a) we can write it as

$$D_1(\phi, \phi_0; \eta_1, \eta_2) = (\eta_1 - \eta_2) K_+(\pi - \phi; \eta_1) K_+(\pi - \phi_0; \eta_1) D_1(\phi, \phi_0; \eta_2) \quad (40)$$

where $D_1(\phi, \phi_0; \eta_2)$ is defined in (35) and as before η_i is equal to twice the resistivity of the pertinent strip. Since

$$K_+(\pi - \phi; 0) = \sqrt{2} \sin\left(\frac{\pi - \phi}{2}\right) \quad (41)$$

(40) is seen to reduce to (36) when $\eta_1 = 0$ and the angles are referenced with respect to the metallic face as is the case with (36).

The doubly diffracted field associated with the mechanism illustrated in Figure 5(b) can be derived by following the procedure described in [2]. However, because $D_1(\phi, \phi_0; \eta_1, \eta_2)$ differs from the diffraction coefficient of the isolated resistive half plane only by a certain factor (non-vanishing when $\phi = 0$), the contribution of the double diffraction mechanism illustrated in Figure 5(b) can be easily related to that of the isolated resistive strip treated in [2]. In particular we find that

$$D_{21}(\phi_2, \phi_0; \eta_1, \eta_2, \eta_3) = \{[(\eta_1 - \eta_2) K_+(\pi; \eta_1) K_+(\pi - \phi_0; \eta_1)] \quad (42) \\ [(\eta_3 - \eta_2) K_+(\pi - \phi_2; \eta_3) K_+(\pi; \eta_3)]\} D_{21}(\phi_2, \phi_0; \eta_2)$$

where $D_{21}(\phi_2, \phi_0; \eta_2)$ is the double diffraction coefficient for the isolated strip appearing in (37). Since

$$K_+(\phi; \eta \rightarrow \infty) = \frac{1}{\sqrt{\eta}} \quad (43)$$

it can be readily shown that

$$D_{21}(\phi_2, \phi_0; \eta_1 \rightarrow \infty, \eta_2, \eta_3 \rightarrow \infty) = D_{21}(\phi_2, \phi_0; \eta_2).$$

The diffraction coefficient associated with the triple diffraction mechanism shown in Figure 5(c) can be also related to the corresponding one for the

isolated resistive strip. Specifically, we find that

$$\begin{aligned}
D_{121}(\phi, \phi_0; \eta_1, \eta_2, \eta_3) = & [(\eta_1 - \eta_2) K_+(\pi; \eta_1) K_+(\pi - \phi_0; \eta_1)] \\
& [(\eta_3 - \eta_2) K_+(\pi; \eta_3) K_+(\pi; \eta_3)] \\
& [(\eta_1 - \eta_2) K_+(\pi - \phi; \eta_1) K_+(\pi; \eta_1)] D_{121}(\phi, \phi_0; \eta_2)
\end{aligned} \tag{44}$$

where $D_{121}(\phi, \phi_0; \eta_2)$ denotes the same diffraction coefficient appearing in (38). As expected, on using (43) we find that

$$D_{121}(\phi, \phi_0; \eta_1 \rightarrow \infty, \eta_2, \eta_3 \rightarrow \infty) = D_{121}(\phi, \phi_0; \eta_2).$$

The triple diffraction mechanism illustrated in Figure 5(d) does not relate to any of the mechanisms existing on a single strip. Also, the procedure given in [2] is not applicable for the derivation of the diffracted field associated with this mechanism. The primary reason for this is the vanishing diffraction coefficient at Q_2 which requires that a double spectral integral is formulated and evaluated via the steepest descent method. This is beyond the scope of the present study and will be considered in the future. Thus, in computing the diffracted field from the two-strip configuration in Figure 6, we will only consider the contributions of the mechanisms shown in Figures 5(a)–(c).

Taking the origin (phase reference) of the geometry to be at Q_3 we find that the contribution of all first order diffraction mechanisms is

$$\begin{aligned}
E_{z1}^d(\rho, \phi) = & \frac{e^{jk_0\rho}}{\sqrt{\rho}} \left\{ D_1(\phi, \phi_0; \infty, \eta_2) e^{-jk_0(w_2+w_3)(\cos\phi+\cos\phi_0)} \right. \\
& + D_1(\phi, \phi_0; \eta_2, \eta_3) e^{-jk_0 w_3(\cos\phi+\cos\phi_0)} \\
& \left. + D_1(\phi, \phi_0; \eta_3, 0) \right\}
\end{aligned} \tag{45}$$

where $D_1(\phi, \phi_0; \eta_1, \eta_2)$ is the coefficient defined in (40). For the doubly diffracted fields we have

$$\begin{aligned}
E_{z2}^d(\rho, \phi) = & \frac{e^{jk_0\rho}}{\sqrt{\rho}} \left\{ D_{21}(\pi - \phi, \phi_0; \infty, \eta_2, \eta_3) e^{-jk_0[(w_2+w_3)\cos\phi_0+w_3\cos\phi]} \right. \\
& + D_{21}(\phi, \pi - \phi_0; \eta_3, \eta_2, \infty) e^{-jk_0[w_3\cos\phi+(w_2+w_3)\cos\phi_0]} \\
& + D_{21}(\pi - \phi, \phi_0; \eta_2, \eta_3, 0) e^{-jk_0 w_3\cos\phi_0} \\
& \left. + D_{21}(\phi, \pi - \phi_0; 0, \eta_3, \eta_2) e^{-jk_0 w_3\cos\phi} \right\}
\end{aligned} \tag{46}$$

representing the contribution of the two double diffraction mechanisms on each strip. Finally, the triply diffracted field associated with pairs of adjacent edges is given by

$$\begin{aligned}
E_{z3}^d(\rho, \phi) = \frac{e^{jk_0\rho}}{\sqrt{\rho}} \Big\{ & D_{121}(\phi, \phi_0; \infty, \eta_2, \eta_3) e^{-jk_0(w_2+w_3)(\cos\phi+\cos\phi_0)} \\
& + D_{121}(\pi-\phi, \pi-\phi_0; \eta_3, \eta_2, \infty) e^{-jk_0w_3(\cos\phi+\cos\phi_0)} \\
& + D_{121}(\phi, \phi_0; \eta_2, \eta_3, 0) e^{-jk_0w_3(\cos\phi+\cos\phi_0)} \\
& + D_{121}(\pi-\phi, \pi-\phi_0; 0, \eta_3, \eta_2) \Big\} \quad (47)
\end{aligned}$$

with D_{121} as defined in (44).

As in the previous section, the total diffracted field (up to and including third order contributions) is obtained from (39).

7 Results and Validation

A first step before the presentation of any results is the validation of the moment method solution described in Section 3. Once validated, this solution could then serve as a reference for evaluating the accuracy and limitations of the small width and high frequency approximations.

Our moment method solution was validated by comparison with data from an alternate simulation which avoided use of the half plane Green's function. In this simulation, the metallic half plane was modeled by a long strip (suppression card) whose resistivity profile is illustrated in Figure 7. As seen, the left portion of the strip is metallic whereas its right side is resistive with its resistivity increasing quadratically until it reaches 60 Ω at the rear termination of the strip. This profile was carefully selected through an examination of its pulse response and was found to sufficiently suppress scattering contributions from the strip's rear edge. Consequently, it permits a simulation of the metallic half plane except perhaps for observation and incidence angles near its surface. Comparisons of results generated via the moment method solution described in Section 3 and that associated with the suppression card are illustrated in Figure 8. These represent a sample among the numerous comparisons involving a variety of resistive strip extensions. As seen, the moment method solution using the half plane Green's function is in good agreement with the data based on the suppression card model.

Any minor differences can be attributed to undesired contributions from the tapered side of the suppression card. Needless to mention, our moment method solution based on the half plane Green's function was usually more than 20 times faster than that based on the suppression card.

Having demonstrated the validity of our MM solution described in Section 3, we now proceed to examine the accuracy and limitations associated with our approximate small width and high frequency solutions. To do so we concentrated on a single strip extension (see Figure 4) and examined each solution as a function of the strip's width for different values of the resistivity R_e . Comparisons of data from the two approximate solutions with those based on the MM are illustrated in Figure 9 for $\phi = \phi_0 = 120^\circ$ and in Figure 10 for $\phi = \phi_0 = 180^\circ$. Each of these figures displays six backscatter echowidth curves plotted as a function of the strip's width and corresponding to different resistivities chosen to span a wide range of values from small and real to large and complex. An obvious and expected observation from these comparisons is that the small width approximation predicts the correct echowidth for $w \ll \lambda$ whereas the high frequency solution does the same for large w .

Additional echowidth curves as a function of angle are given in Figures 11–13 corresponding to strip extensions of different widths and resistivities. Again for $w = 0.1\lambda$ (see Figure 11) the small width approximation is seen to be in excellent agreement with the exact solution regardless of the value of R_e , even when $\text{Im}(R_e) > 0$, in which case the resistive strip supports a surface wave. Also, as demonstrated in Figure 12, when $w = 0.5\lambda$ the high frequency solution is identical to the exact for real or complex strip resistivities, even when these are chosen to support surface waves. The curves in Figure 13 provide us with additional confidence that the high frequency solution can be used for widths as small as $\lambda/10$.

As can be expected, the small width approximation improves with decreasing w whereas the high frequency solution becomes more accurate as the width of the extension increases. However, it is apparent from the above comparisons that the resistivity of the extension plays some role in the accuracy of each approximation. This is particularly so for edge-on incidence and backscatter observations, a situation which is most demanding for both approximations. For most cases the small width approximation can be used for $w < \lambda/5$ whereas the high frequency solution can be used down to $w = \lambda/10$. An exception to this is the case of near edge-on incidence and backscatter

observation and only for certain values of R_e . As illustrated in the echowidth comparisons displayed in Figure 10, when the magnitude of R_e is near 0.5, the high frequency approximation breaks down when the width is less than 0.3λ . Also, for very small values of R_e the small width approximation cannot be stretched beyond $\lambda/10$ due to the different behavior of the strip current for those values of R_e . Fortunately, though, we found that in those cases the validity of one of the approximations can be extended to permit an overlap. Thus, in general, the two approximations are sufficient for characterizing the scattering of all uniform resistive strip extensions regardless of width, incidence angle and associated resistivity. Needless to mention, the CPU time associated with these approximations is trivial.

For sheet extensions comprised of strips having different resistivities, the high frequency solution can be employed in a straightforward manner but may prove tedious (not necessarily time-consuming) when more than three strips are involved. In contrast the implementation of the MM/Green's function solution remains unchanged, and this solution is thus best suited for extensions having arbitrary resistivity profiles. An example illustrating a comparison between the two-strip extension high frequency solution with the exact MM/Green's function solution is shown in Figure 14. We remark that the given high frequency solution for the two-strip extension is not valid for $\phi_0 > 160^\circ$ unless additional higher order terms are added as discussed in Section 6.

References

- [1] E.H. Newman, "TM Scattering by a Dielectric Cylinder in the Presence of a Half Plane," *IEEE Trans. Antennas Propagat.*, Vol. AP-33, July 1985, pp. 773-782.
- [2] M.I. Herman and J.L. Volakis, "High-frequency scattering by a resistive strip and extensions to conductive and impedance strips," *Radio Science*, Vol. 22, May-June 1987, pp. 335-349.
- [3] G. Uzgören, A. Büyükaksoy and A.H. Serbest, "Diffraction coefficient related to a discontinuity formed by impedance and resistive half planes," *IEE Proceedings*, Vol. 136, pt. H, Feb. 1989, pp. 19-23.

- [4] T.B.A. Senior, "Diffraction by a Material Junction," University of Michigan Radiation Laboratory Report RL-880, June 1990.
- [5] P.C. Clemmow, "A note on the diffraction of a cylindrical wave by a perfectly conducting half plane," *Quart. J. Mech. and Applied Math.*, Vol. III, pt. 3, 1950, pp. 377-384.
- [6] J.J. Bowman, T.B.A. Senior and P.L.E. Uslenghi, *Electromagnetic and Acoustic Scattering by Simple Shapes*, Hemisphere Pub. Co., New York, 1987 (p. 311).
- [7] P.C. Clemmow, *The Plane Wave Spectrum Representation of Electromagnetic Fields*, Pergamon Press: New York, 1966 (pp. 51-55).
- [8] R.G. Kouyoumjian and P.H. Pathak, "A uniform geometrical theory of diffraction for an edge in a perfectly conducting surface," *Proceedings of the IEEE*, Vol. 62, Nov. 1974, pp. 1448-1461.

List of Figures

- Figure 1. Geometry of the metallic half plane with a resistive sheet extension.
- Figure 2. Magnitude of the numerically computed (exact) current distribution on the half plane strip extension for different resistivities. (a) $\phi_0 = 60^\circ$; (b) $\phi_0 = 130^\circ$.
- Figure 3. Plots of the integrals $I(\chi; w)$ as a function of w for $\chi = \frac{w}{4}$, $\frac{w}{2}$ and $\frac{3w}{4}$. (a) Real part; (b) imaginary part.
- Figure 4. Illustration of the first order diffraction mechanisms.
- Figure 5. Diffraction mechanisms associated with sheet extensions comprised of multiple resistive strips: (a) single diffraction; (b) double diffraction; (c) triple diffraction; (d) triple diffraction involving three junctions.
- Figure 6. Illustration of a resistive sheet extension to a metallic half plane comprised of two constant resistivity strips.
- Figure 7. Resistivity profile of the suppression card used to replace the metallic half plane.
- Figure 8. Comparison of backscatter echowidth patterns computed via the moment method using either the suppression card or the half plane Green's function. (a) Edge-on incidence echowidth plotted as a function of frequency for a strip having $R_e = 0.5$. (b) Echowidth as a function of angle for 1λ strip having $R_e = 0.5$.
- Figure 9. Comparison of backscatter echowidths based on the small width and high frequency approximations with corresponding moment method (exact) data. The configuration applies to a single strip extension and the curves are plotted as a function of the strip's width with $\phi = \phi_0 = 120^\circ$. Six curves are shown corresponding to different normalized resistivities.

Figure 10. Comparison of backscatter echowidths based on the small width and high frequency approximations with corresponding moment method (exact) data. The configuration applies to a single strip extension and the curves are plotted as a function of the strip's width with $\phi = \phi_0 = 180^\circ$. Six curves are shown corresponding to different normalized resistivities.

Figure 11. Comparison of backscatter echowidths as computed by the small width approximation and the moment method. The configuration is a single strip extension of width $\lambda/10$ and each of the four curves corresponds to a different value of R_e . All curves are plotted as a function of angle.

Figure 12. Comparison of backscatter echowidth curves as computed by the high frequency approximation and moment method. The configuration is a single strip extension of width $w = \lambda/2$, and each of the three curves corresponds to a different resistivity. All curves are plotted as a function of angle.

Figure 13. Comparison of backscatter echowidth curves as computed by the high frequency approximation and moment method. The configuration is a single strip extension having a normalized resistivity of $R_e = 0.75$, and each of the three curves corresponds to a different width. All curves are plotted as a function of angle.

Figure 14. Comparison of backscatter echowidths based on the moment method (numerical) and high frequency approximation for a two part card where the cards have resistivities as shown in the inset. (a) Echowidth as a function of angle where each card is 0.5λ wide. (b) Echowidth at 180° incidence as a function of card width.

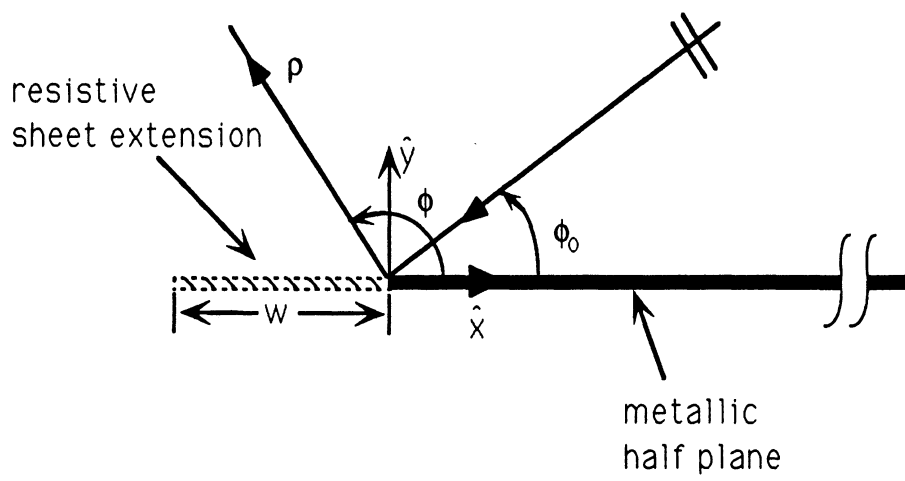
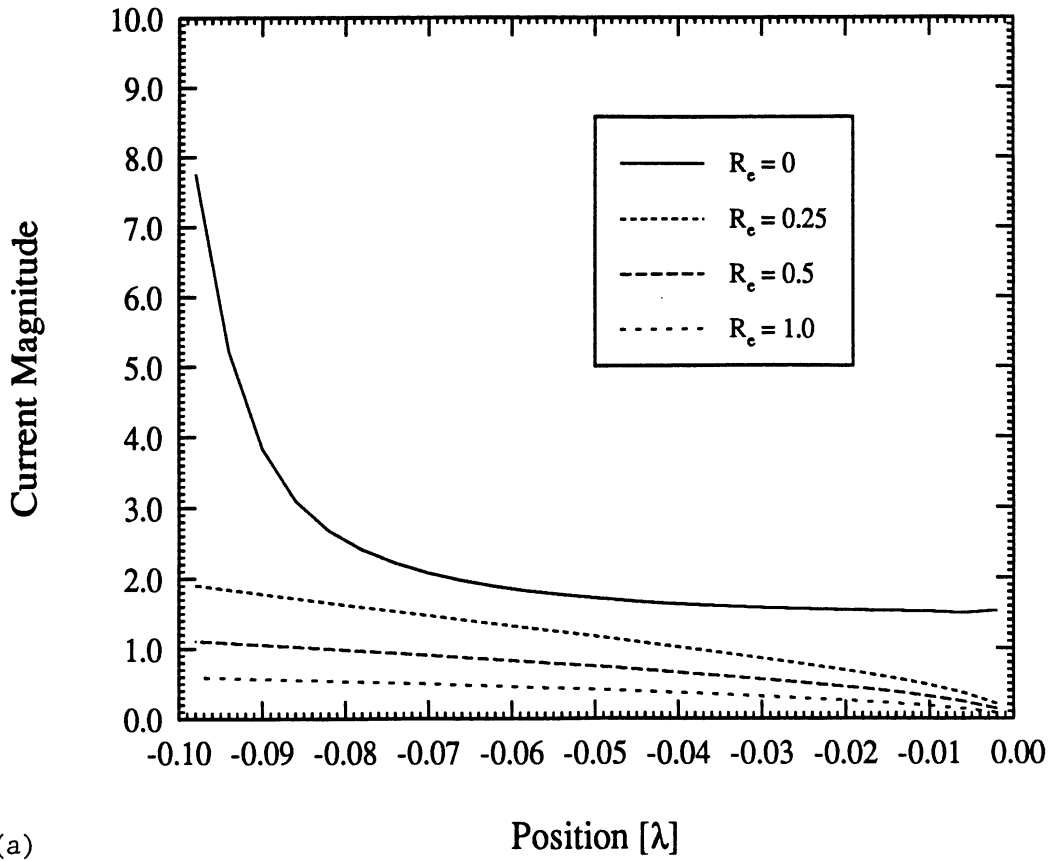


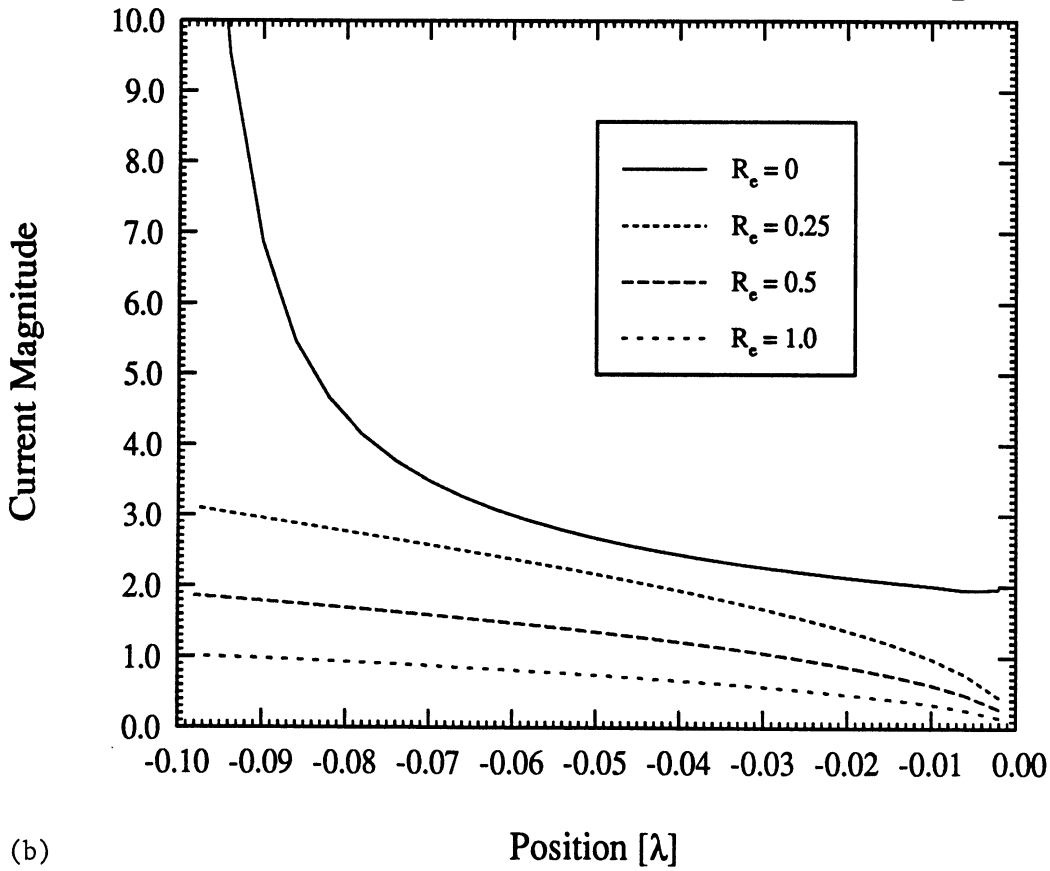
Figure 1. Geometry of the metallic half plane with a resistive sheet extension.

Current on 0.1λ edge card at $\phi = 60$ [E_z]



(a)

Current on 0.1λ edge card at $\phi = 130$ [E_z]



(b)

Figure 2. Magnitude of the numerically computed (exact) current distribution on the HP strip extension for different resistivities. (a) $\phi_0 = 60^\circ$; (b) $\phi_0 = 130^\circ$.

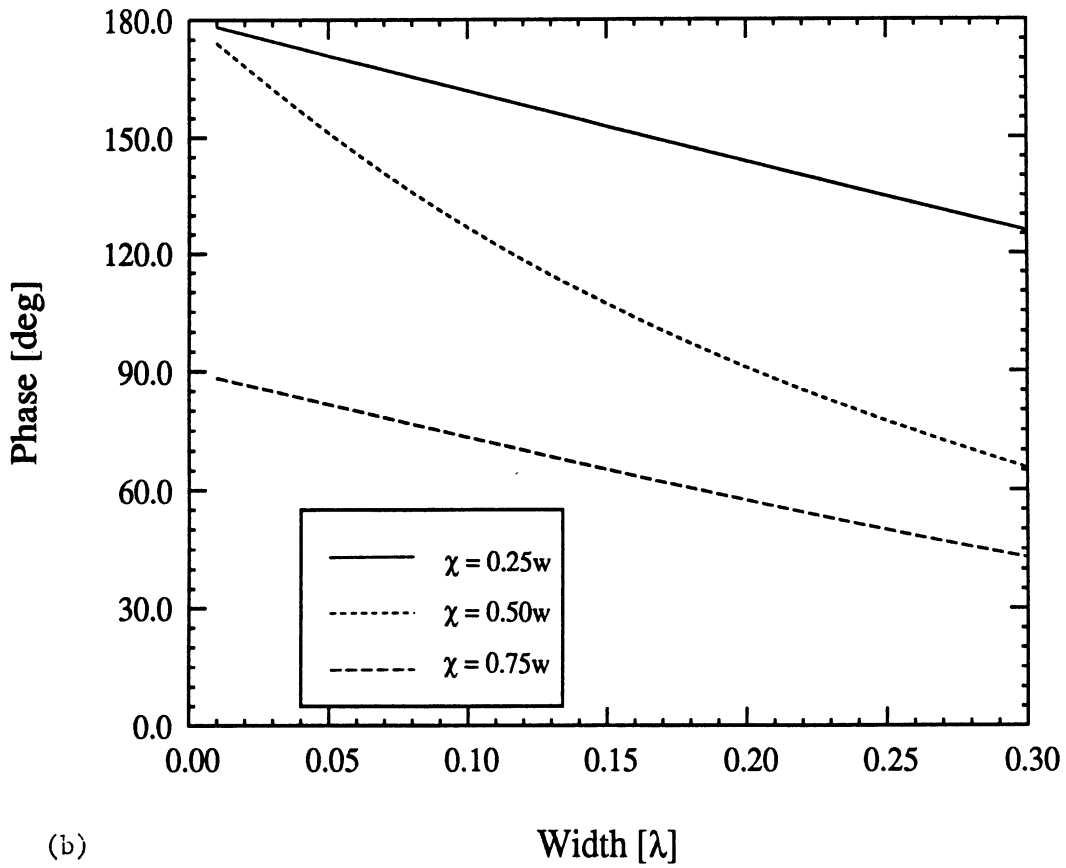
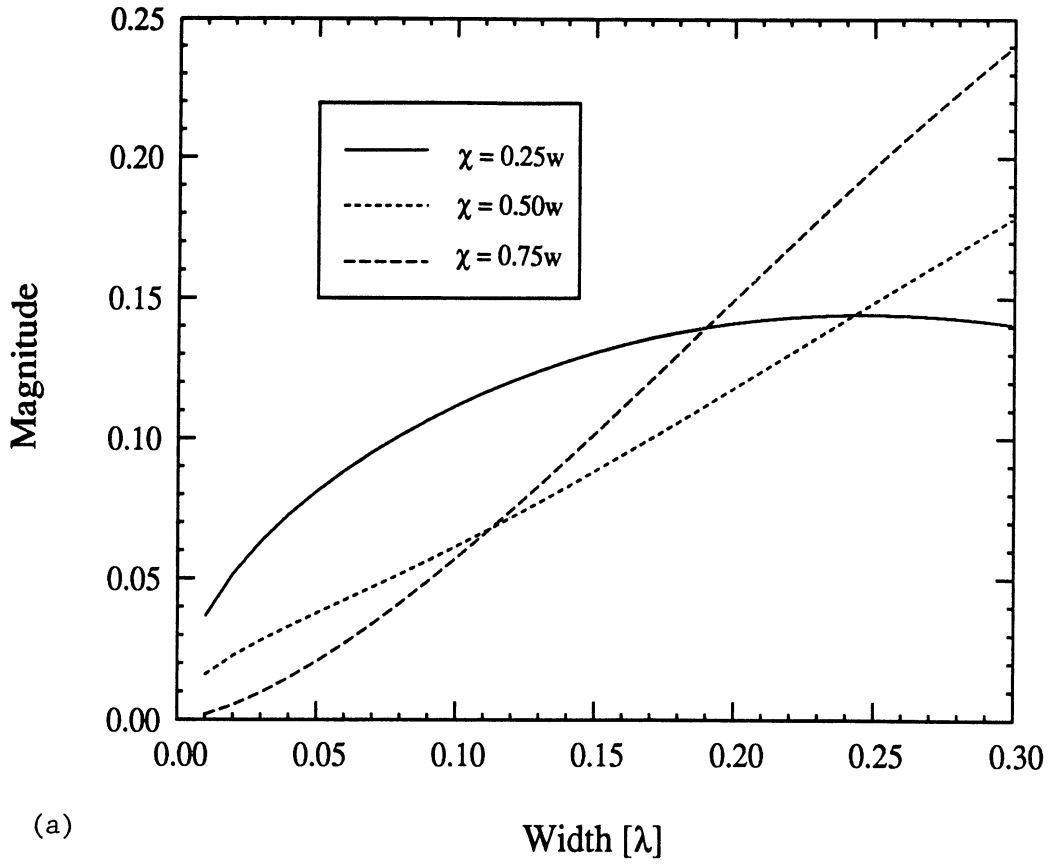


Figure 3. Plots of the integrals $I(\chi; w)$ as a function of w for $\chi = \frac{w}{4}$, $\frac{w}{2}$ and $\frac{3w}{4}$.
(a) Real part; (b) imaginary part.

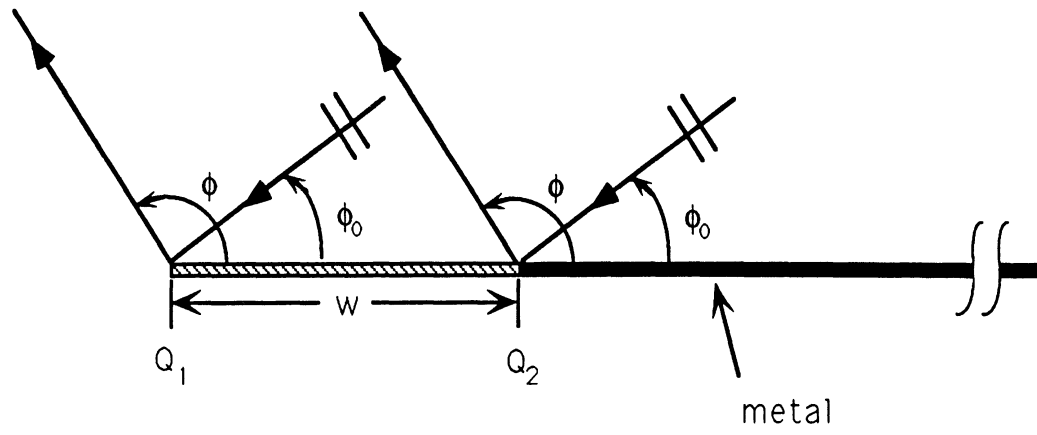


Figure 4. Illustration of the first order diffraction mechanisms.

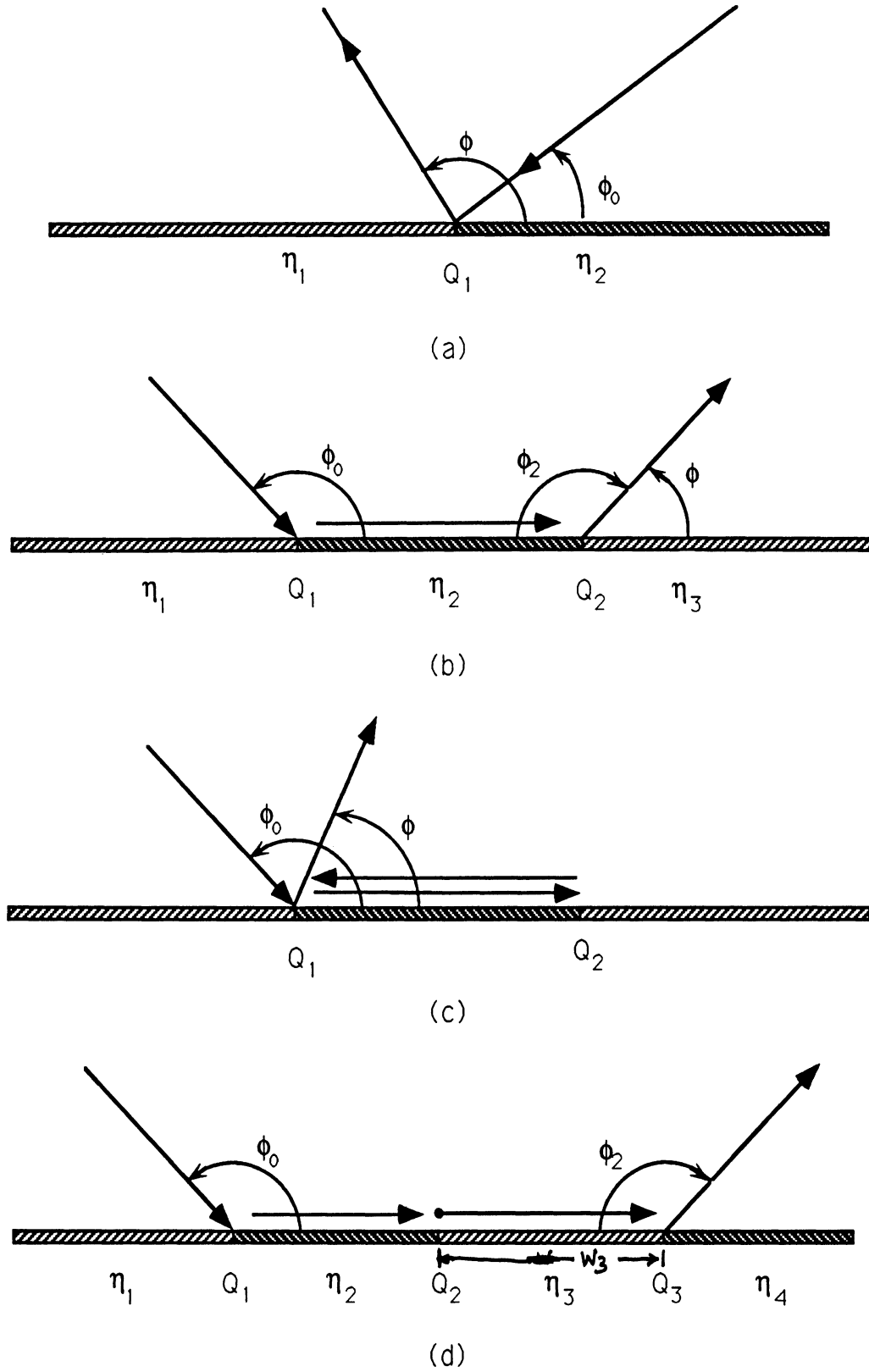


Figure 5: Diffraction mechanisms associated with extension comprised of multiple resistive strips: (a) single diffraction; (b) double diffraction; (c) triple diffraction; (d) triple diffraction involving three junctions.

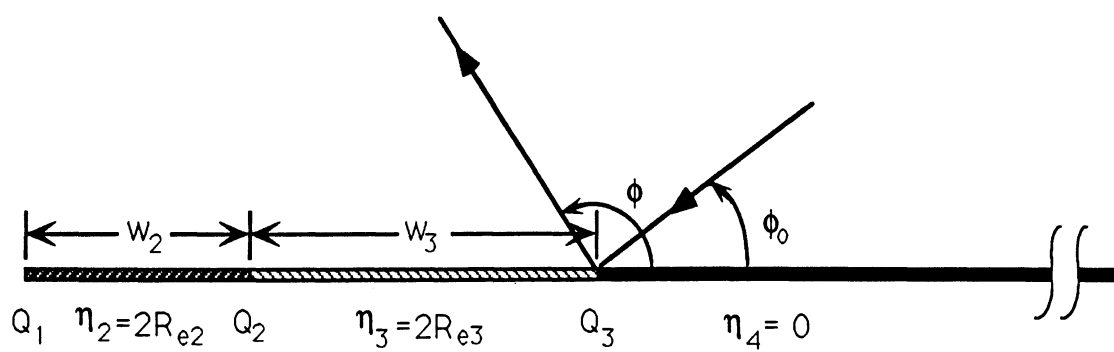


Figure 6. Illustration of a resistive sheet extension to the metallic half plane comprised of two constant resistivity strips.

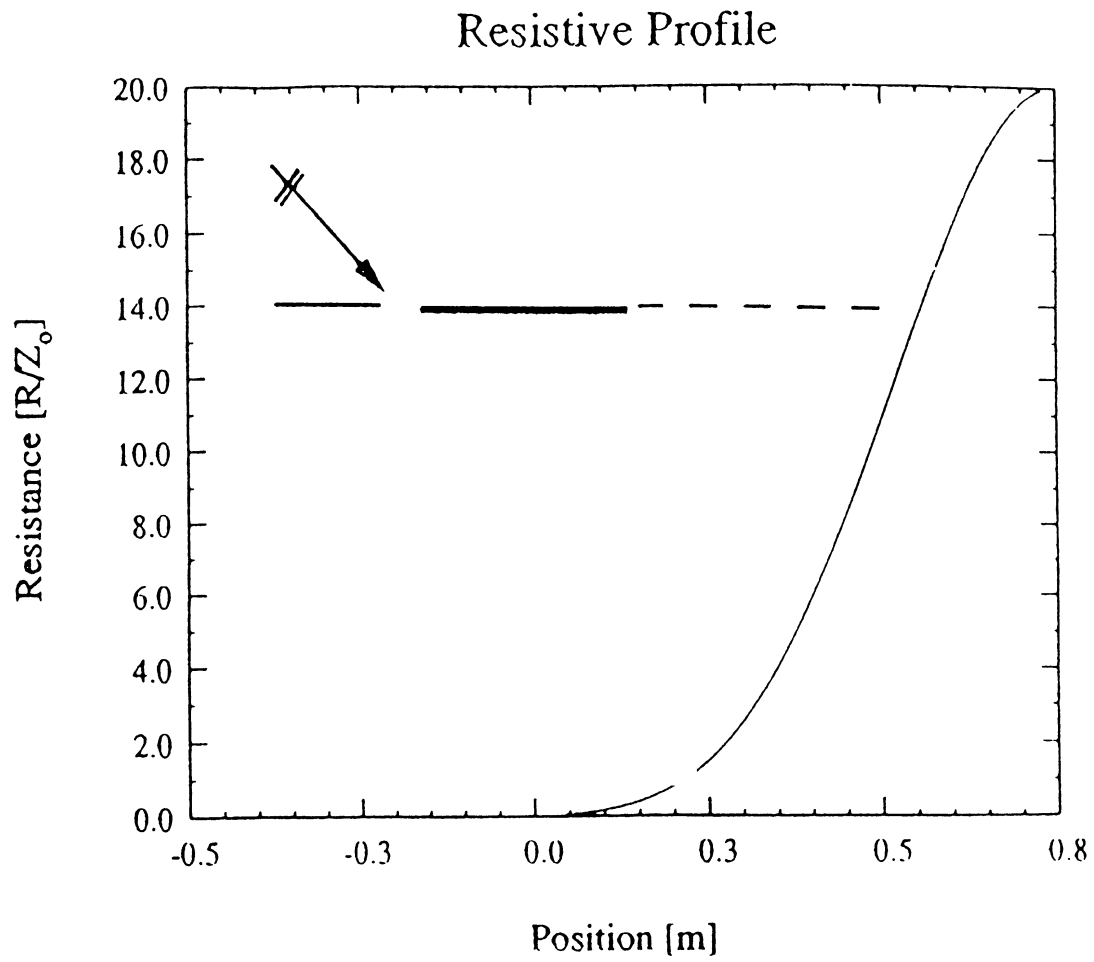
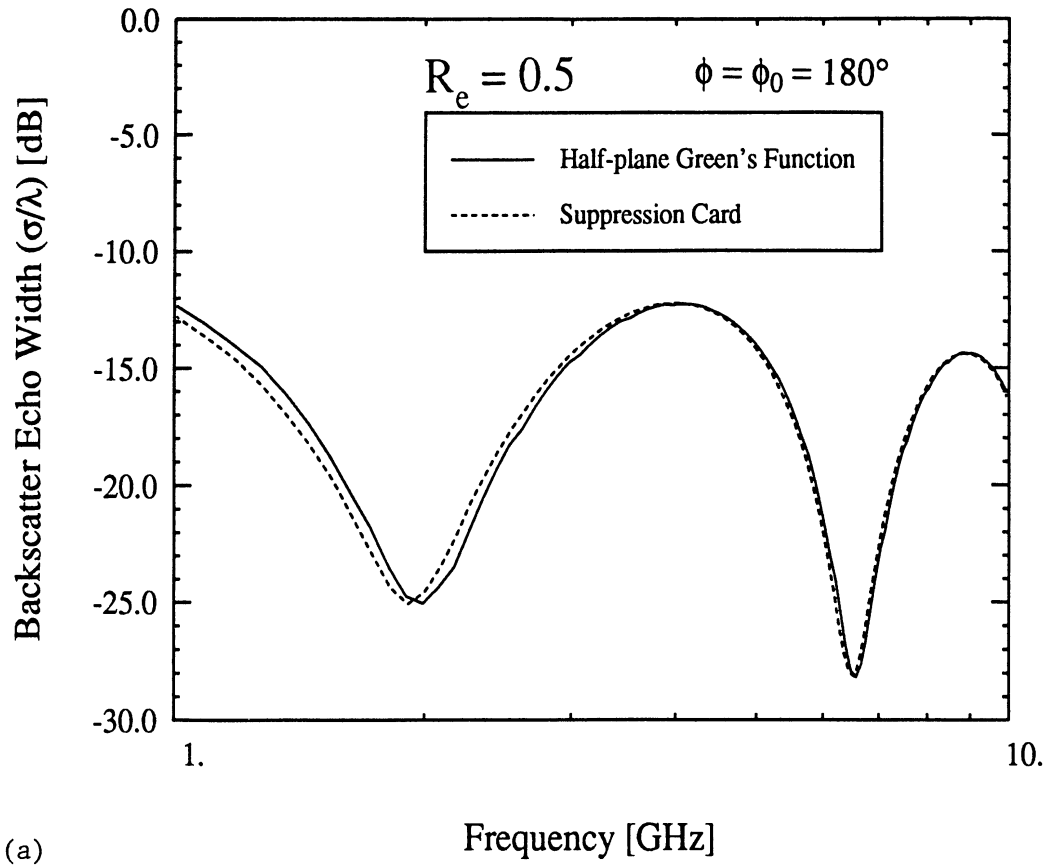
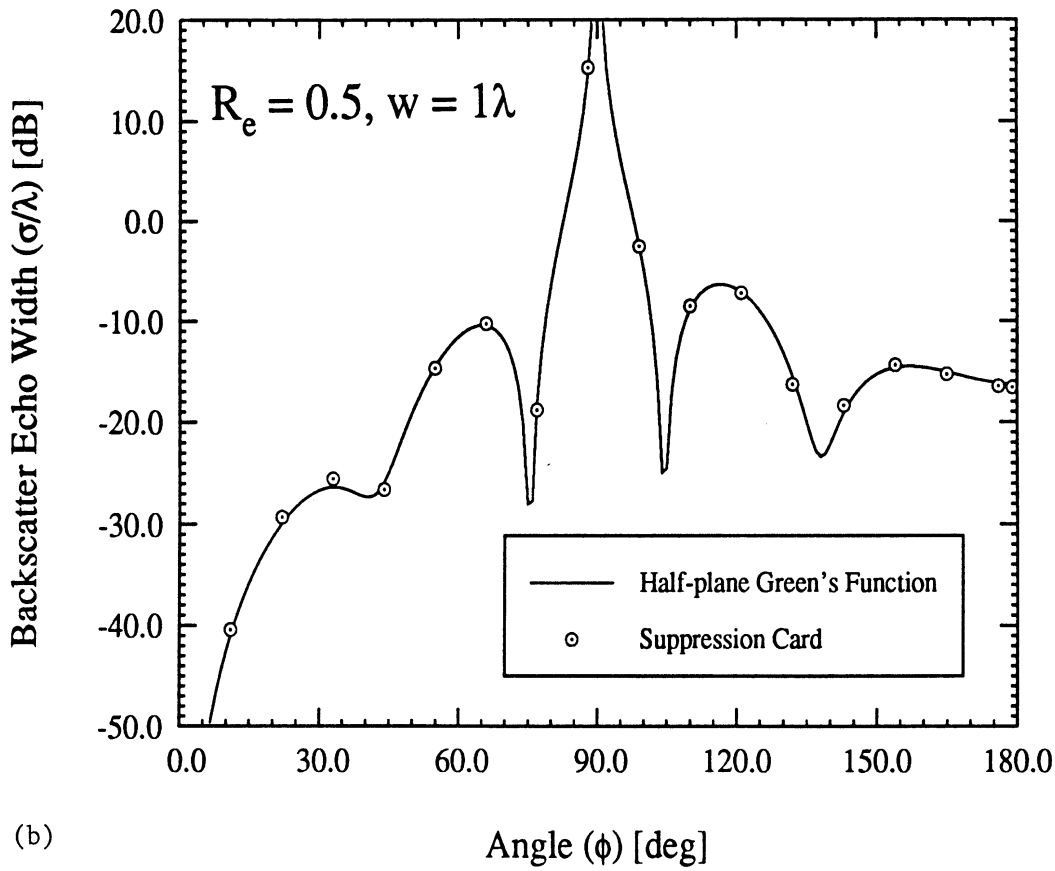


Figure 7. Resistivity profile of the suppression card used to replace the metallic half plane.



(a)



(b)

Figure 8. Comparison of backscatter echowidth patterns computed via the moment method using either the suppression card or the half plane Green's function. (a) Edge-on incidence echowidth plotted as a function of frequency for a strip having $R_e = 0.5$. (b) Echowidth as a function of angle for 1λ strip having $R_e = 0.5$.

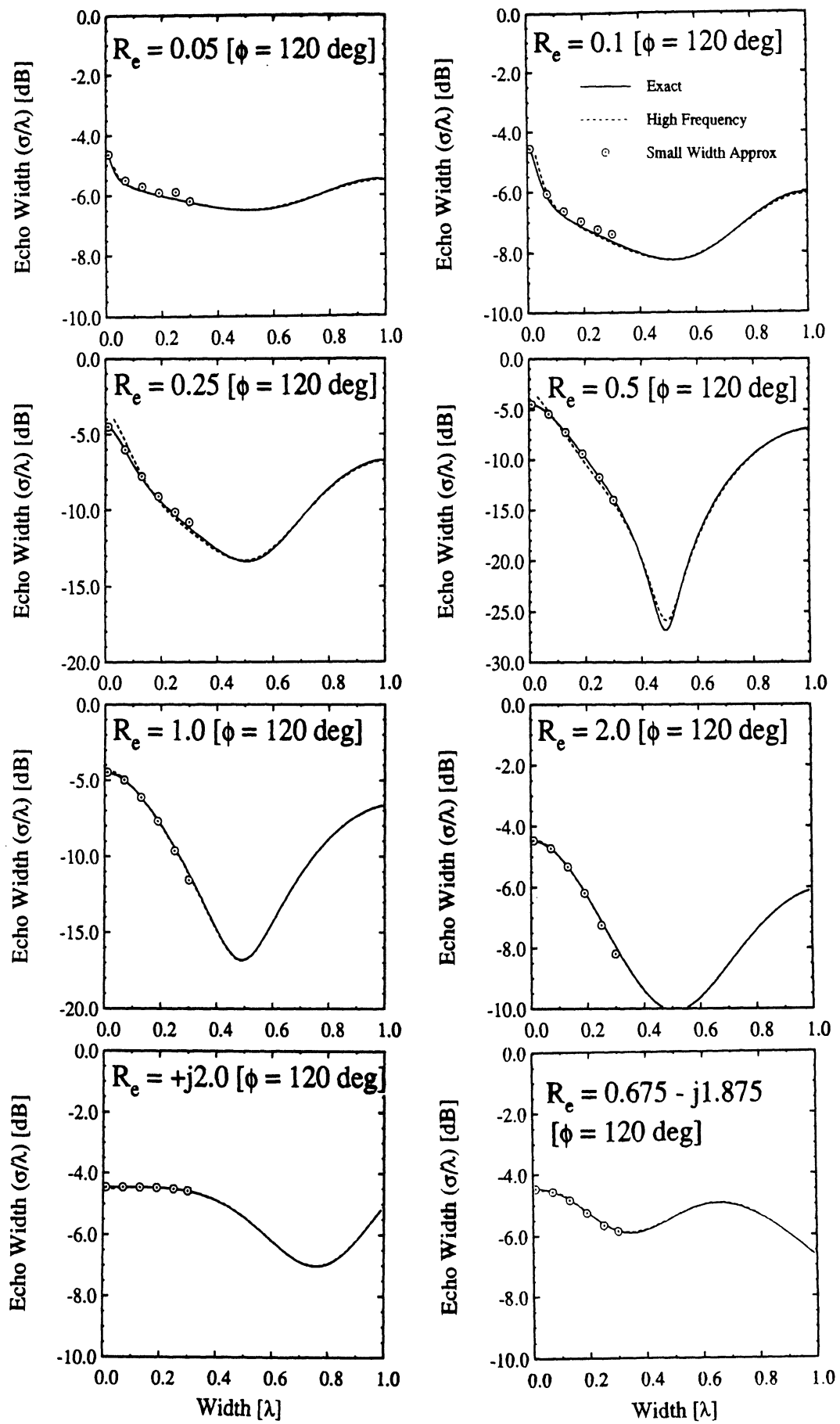


Figure 9. Comparison of backscatter echowidths based on the small width and high frequency approximations with corresponding moment method (exact) data. The configuration applies to a single strip extension and the curves are plotted as a function of the strip's width with $\phi = \phi_0 = 120^\circ$. Six curves are shown corresponding to different normalized resistivities.

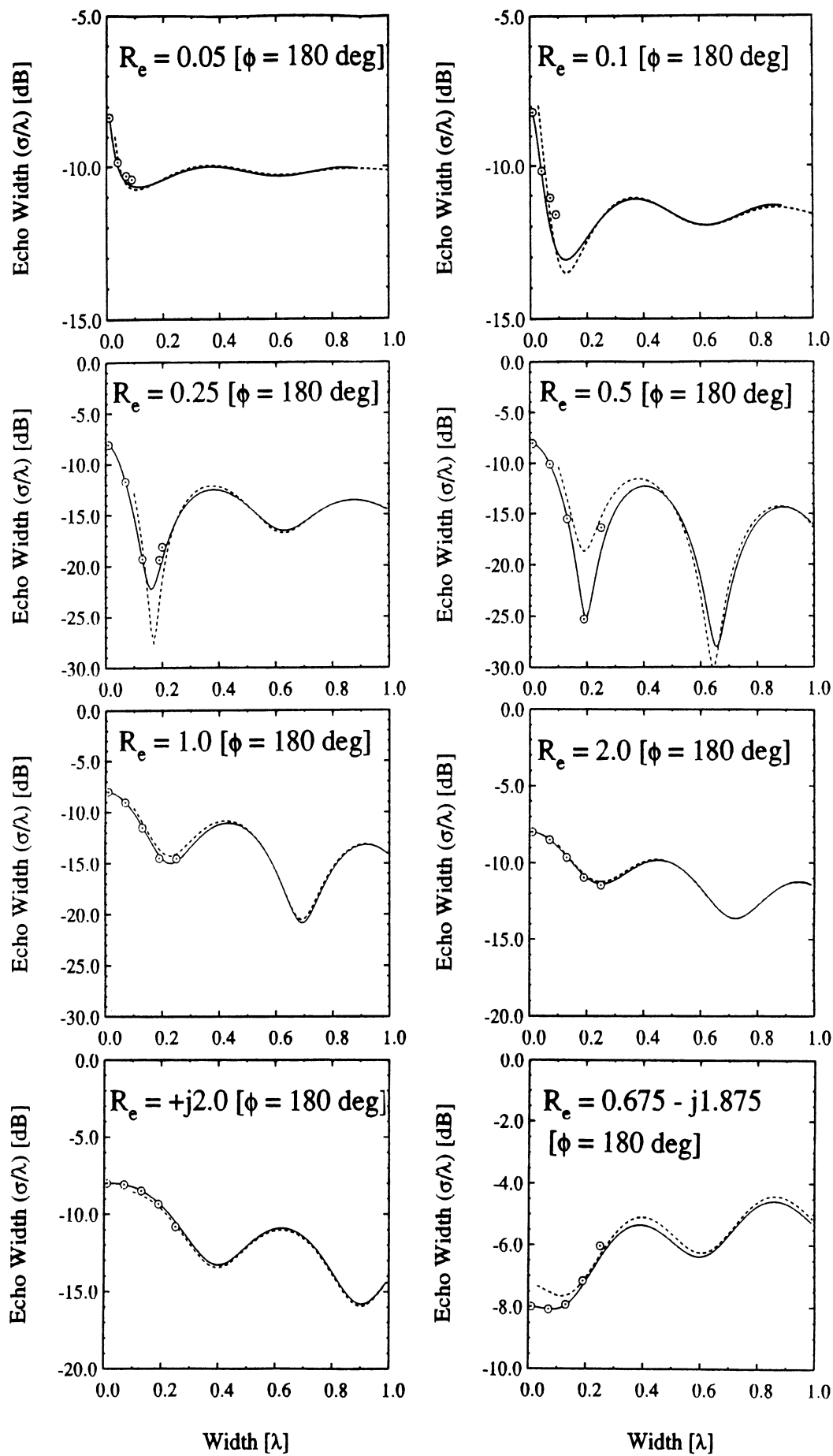


Figure 10. Comparison of backscatter echowidths based on the small width and high frequency approximations with corresponding moment method (exact) data. The configuration applies to a single strip extension and the curves are plotted as a function of the strip's width with $\phi = \phi_0 = 180^\circ$. Six curves are shown corresponding to different normalized resistivities.

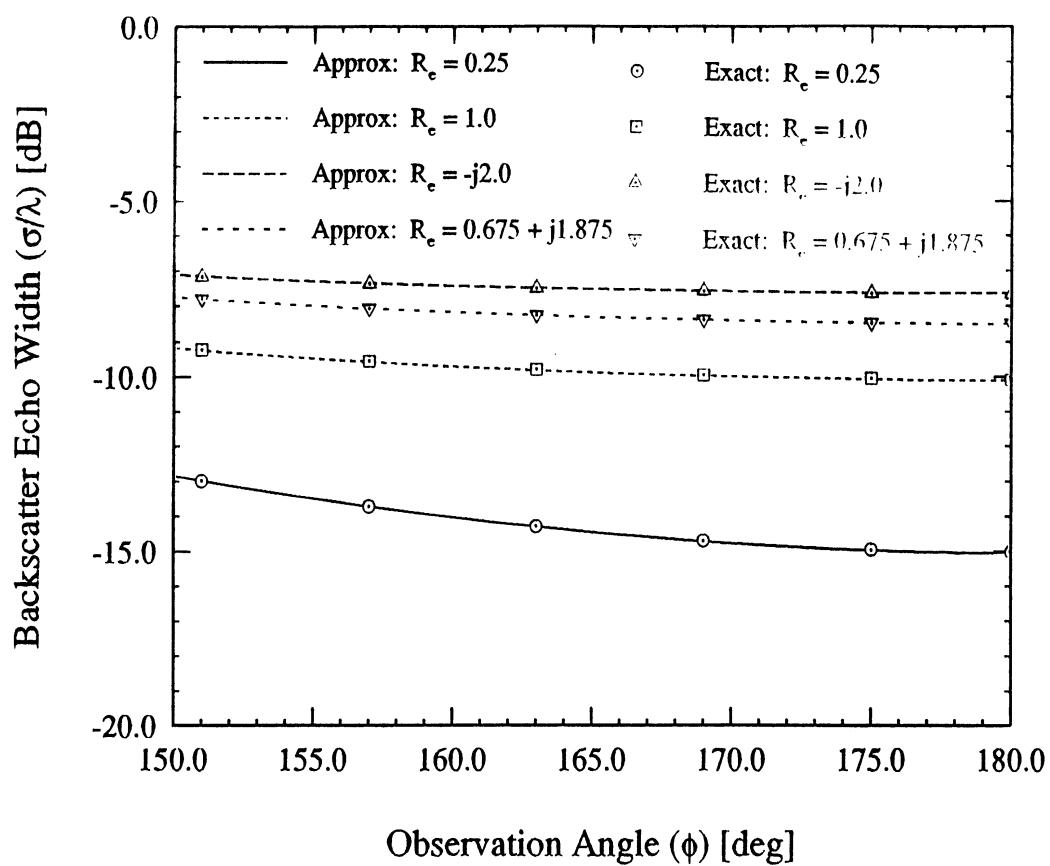


Figure 11. Comparison of backscatter echowidths as computed by the small width approximation and the moment method. The configuration is a single strip extension of width $\lambda/10$ and each of the four curves corresponds to a different value of R_e . All curves are plotted as a function of angle.

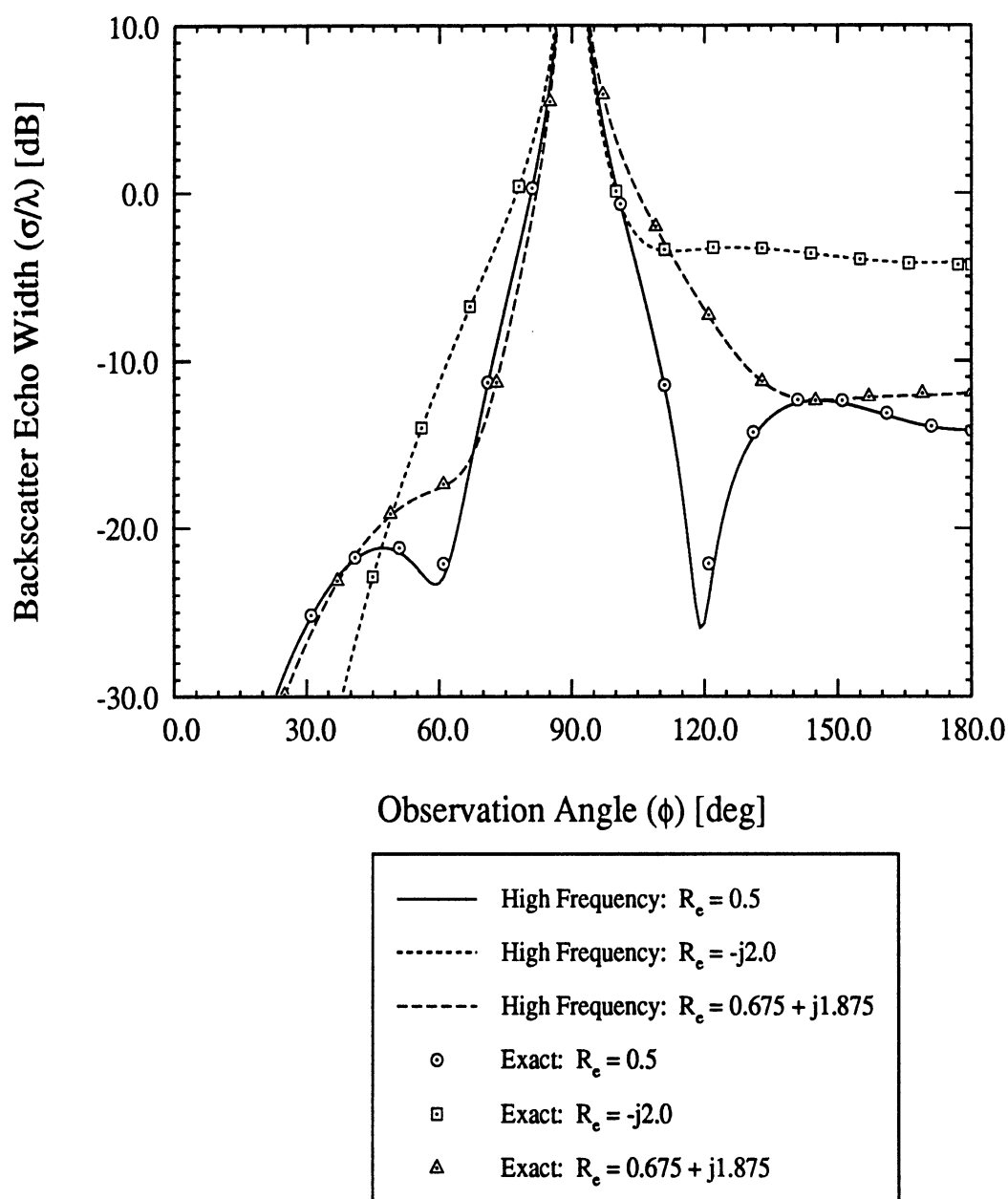


Figure 12. Comparison of backscatter echowidth curves as computed by the high frequency approximation and moment method. The configuration is a single strip extension of width $w = \lambda/2$, and each of the three curves corresponds to a different resistivity. All curves are plotted as a function of angle.

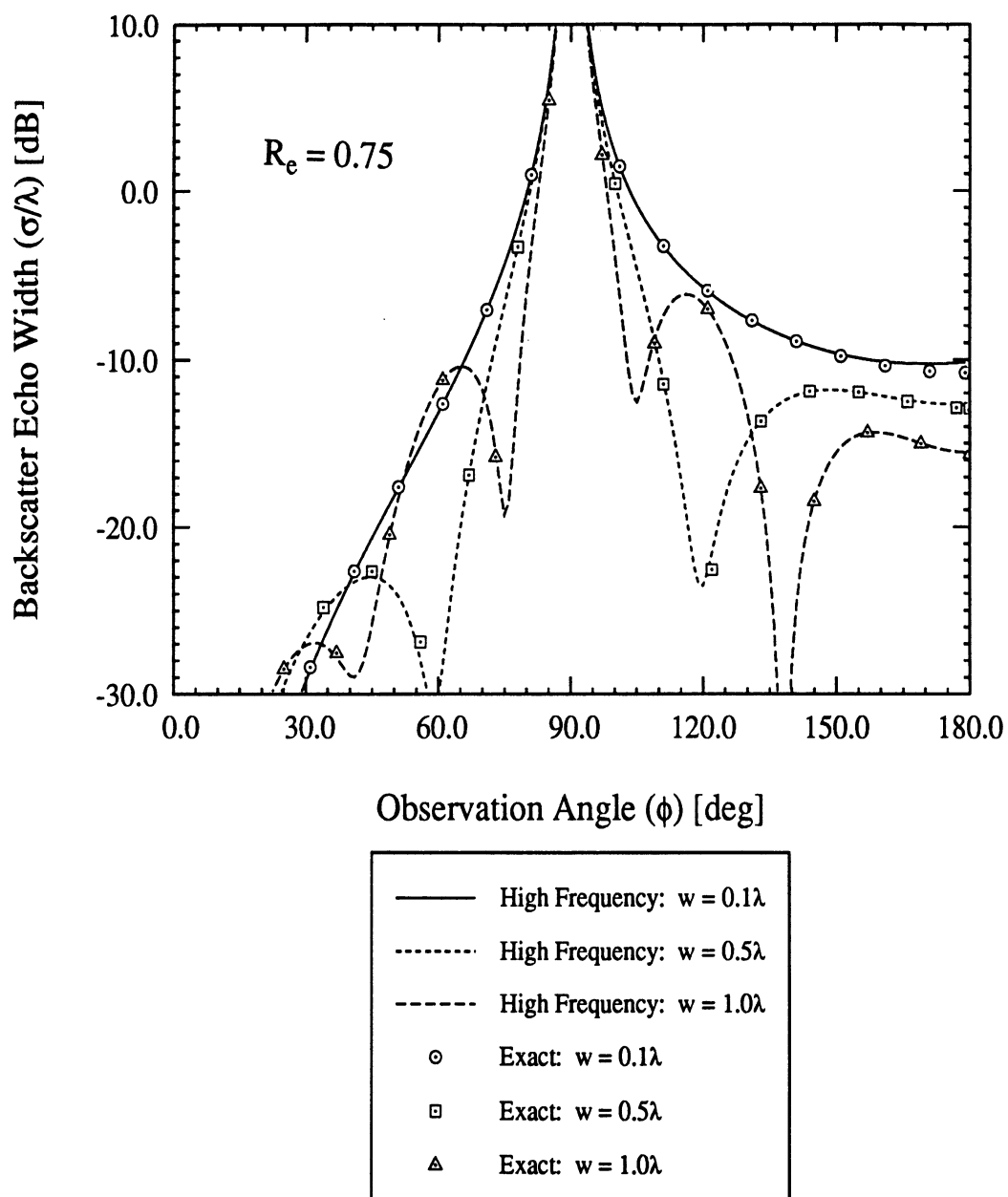


Figure 13. Comparison of backscatter echowidth curves as computed by the high frequency approximation and moment method. The configuration is a single strip extension of width $w = \frac{3}{4}\lambda$, and each of the three curves corresponds to a different resistivity. All curves are plotted as a function of angle.

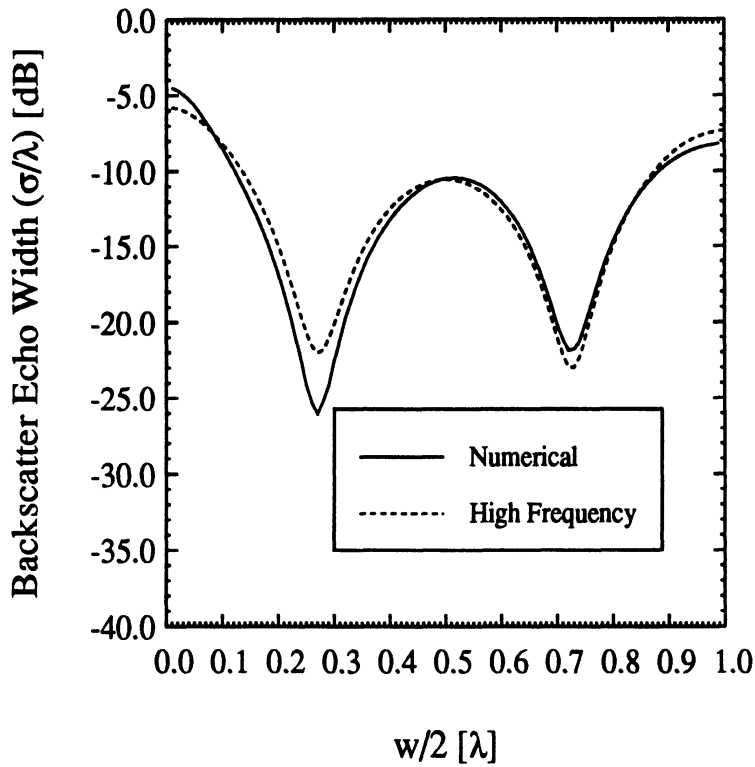
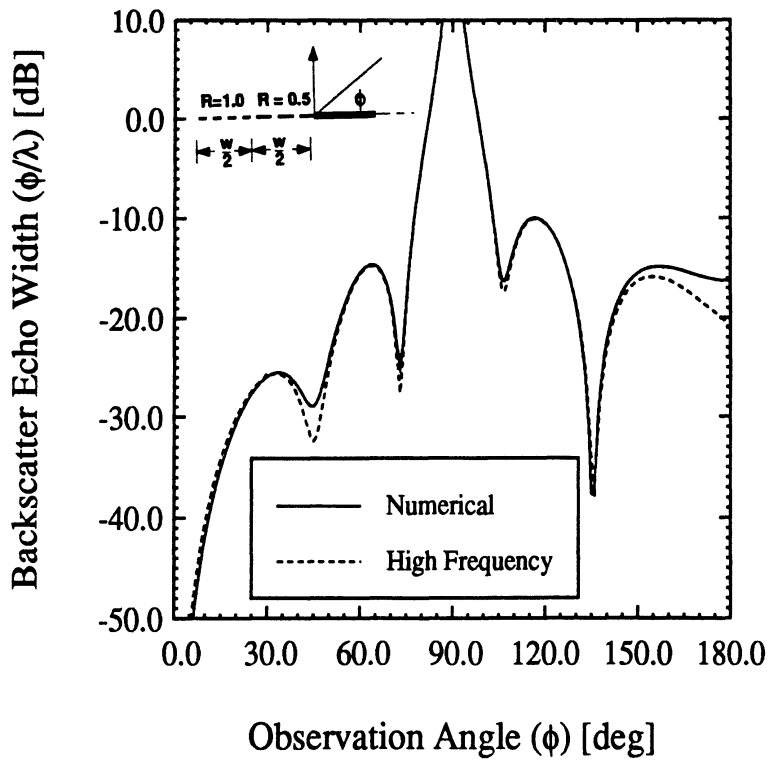


Figure 14. Comparison of backscatter echowidths based on the moment method (numerical) and high frequency approximation for a two part card where the cards have resistivities as shown in the inset. (a) Echowidth as a function of angle where each card is 0.5λ wide. (b) Echowidth at 180° incidence as a function of card width.



3 9015 02527 8048